T.2: Optical Coherence Tomography for Tissue Diagnosis

K Divakar Rao, LBAID
Email: kdivakar@rrcat.gov.in

1. Introduction

Optical coherence tomography (OCT) is an optical analogue of ultrasound imaging and measures backscattered intensity of light rather than sound. Ever since the publication of the first paper by Huang et al in 1991 [1], OCT has emerged as a most powerful biomedical optical imaging modality with depth-sectioning ability down to micrometer-scale for real-time in-vivo imaging of biological tissues [2-5]. OCT is currently used as an established clinical tool for ophthalmic imaging of human eye. Driven by the huge success of OCT in ophthalmology, numerous clinical optical biopsy applications are emerging for 2-D and 3-D imaging of other organs of human body. OCT has several features common to other modalities such as ultrasound and optical microscopy. Compared to clinical ultrasound which can produce images with spatial resolution of ~0.1-1 mm depending on the sound frequency, OCT can acquire 10-20 times sharper images with imaging depths of 1-3 mm depending on the wavelength. On the contrary, confocal microscopy can achieve resolutions down to ~1 μm with depth of imaging of few hundred microns only limited by optical scattering in the tissue. Thus OCT is a powerful tool bridging the gap between microscopy and ultrasound.

2. Principles and different variants of OCT systems:

(i)Time-domain OCT: Figure 1 shows schematic of a time-domain OCT system using a Michelson Interferometer. If the reference arm path is scanned, the interference fringe distribution will vary as a function of time. The fringe intensity will vary periodically over a large path difference for a monochromatic source such as a laser. On the contrary for a low coherence light source, the fringe distribution is observed only for short distances. Thus low-coherence interferometry with reference path length scanning can be used for depth sectioning of samples and this approach is known as time-domain OCT (TDOCT). Assuming a Gaussian spectral intensity distribution of the light source, the detector current integrated over the entire spectrum as a function of the path difference is given as [6],

$$i_d(\Delta l) \approx \sqrt{R_S}\,\exp\left\{-\left[\frac{\Delta l}{l_c / a}\right]^2\right\}\cos(2k_0\Delta l)$$

where Δl is the path difference between the beams, R_S is the sample power reflectivity, l_c is the coherence length of the light source, k_0 is the centre wave number, and $a=2\sqrt{\ln 2}$. As seen above, the interferometric detector signal is a cosine-modulated Gaussian whose full width at half maximum is coherence length l_c (Fig.T.2.1). The plot of demodulated interferometric signal at each depth position forms an axial (longitudinal) scan also known as A-scan. Two dimensional cross sectional images are formed by lining up successive A-scans acquired from different lateral positions on the sample (B-scan), either by scanning the sample arm light or by moving the sample itself.

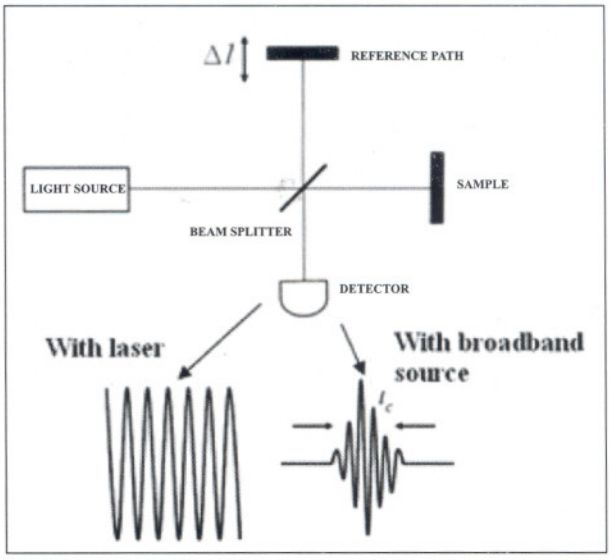

Fig.T.2.1: Schematic of a Time-domain OCT system using a Michelson Interferometer (top) Interference fringe distribution as a function of reference path scan with monochromatic source (bottom left) and broadband source (bottom right)

OCT achieves very high axial image resolution independent of focusing conditions because the axial and transverse resolutions are determined independently. The axial resolution is mainly governed by coherence length of the light source. The coherence length is the spatial width of the field autocorrelation measured by the interferometer. The envelope of the field correlation is equivalent to the Fourier transform of the power spectrum. The axial free-space resolution (Δz), which is the round trip coherence length, is therefore inversely proportional to the spectral bandwidth of the light source and is given by:

$$\Delta z = \frac{2(\ln 2)}{\pi}\frac{\lambda^2}{\Delta\lambda}$$

where $\Delta\lambda$ is the bandwidth and λ is the center wavelength of light source with Gaussian spectral distribution. For example, using a superluminescent diode as light source with λ~830 nm and $\Delta\lambda$~30 nm, depth resolution of ~10 μm can be obtained. Hence using broad bandwidth sources at an optimum wavelength can increase the axial resolution. The axial resolution of OCT imaging is limited by the dispersion in the sample. The actual resolution within the imaged tissue can be estimated by dividing the free space resolution by group refractive index of the biological tissues.

The transverse resolution for OCT imaging is determined by the focused transverse spot size (Δx) of the optical beam. It is defined as $1/e^2$ radius of a Gaussian beam, given by

$$\Delta x = \frac{4\lambda}{\pi}\left(\frac{f}{d}\right) = 1.22\frac{\lambda}{2NA_{obj}}$$

where d is spot size on the objective lens, f is its focal length and NA_{obj} is the numerical aperture of objective lens. Hence transverse resolution is inversely proportional to numerical aperture of the objective. The transverse resolution is also related to the depth of focus or confocal parameter (b) by the relation:

$$b = 2z_R = \frac{\pi\Delta x^2}{2\lambda} = 2\frac{\lambda}{NA_{obj}{}^2}$$

where z_R is Rayleigh range. Figure T.2.2 shows the trade-off between the high lateral resolution and depth of focus. Low numerical aperture (NA) optics give a bigger spot size (poor lateral resolution) and higher depth of focus. On the contrary, high NA optics give high lateral resolution with reduced depth of focus.

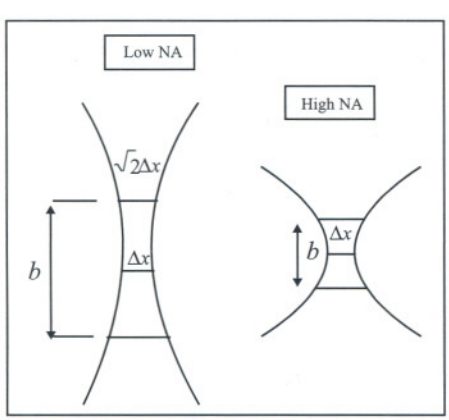

Fig T.2.2. Trade-off between the focal spot size and depth of focus

OCT can achieve high detection sensitivity because interferometry measures the field rather than the intensity of light. This technique is closely related to the heterodyne detection in optical communications. Weak backscattered optical signals are effectively multiplied by the reference signal. Typical TDOCT systems achieve detection sensitivities of 10^{-10} of incident optical power (100dB). This is sufficient to detect optical signals from the depths of 1 to 2 mm in most scattering biological tissues.

The sensitivity of the TDOCT setup, characterized by the signal to noise ratio (SNR) in the shot-noise limit, is given by the ratio of mean square of the interferometric signal to the noise variance and is expressed as

$$SNR_{TDOCT} = \frac{\langle i_d \rangle^2}{\sigma^2} = \frac{\rho S_{TDOCT} R_S}{2eB_{TDOCT}}$$

where i_d is the interferometric signal, σ^2 is the noise variance. S_{TDOCT} is the instantaneous source power, e is the electronic charge, ρ is the detector responsivity, R_S is the sample reflectivity, and B_{TDOCT} is the noise equivalent electronic bandwidth of the detector. As can be seen from this, keeping SNR identical, higher incident powers on the sample are required for high speed imaging compared to slow-speed imaging.

(ii) Fourier domain OCT (FDOCT):

The fundamental limitation of TDOCT is that all depths in the sample are illuminated, but data is only collected from one depth at a time sequentially, by scanning the reference mirror. This inefficiency gets worse as one goes for a deeper scan and also with high axial resolution. The FDOCT scheme simultaneously detects the interferometric signal from all depths without the need for scanning the reference arm. This not only eliminates moving parts in reference arm scanning but also enhances image acquisition speed. FDOCT is implemented in two approaches: spectral domain OCT (SDOCT) and swept source OCT (SSOCT) which are described below.

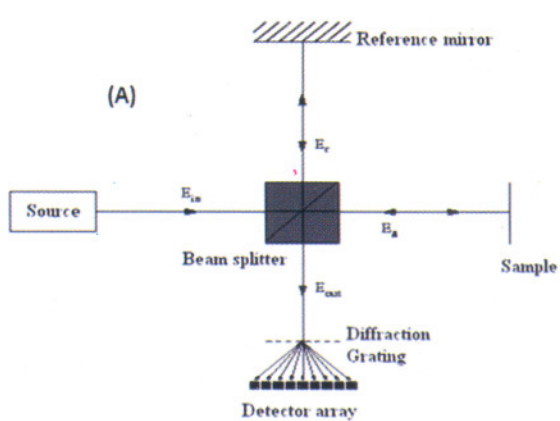

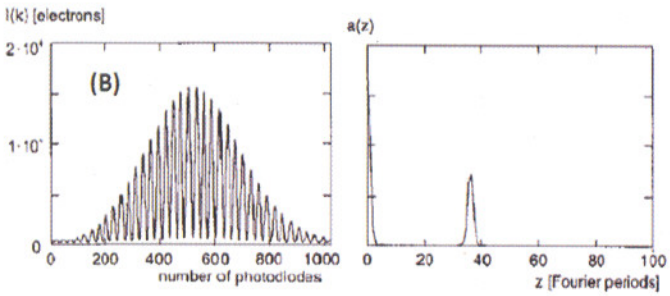

Fig.T.2.3. (A)Schematic of spectrometer based Fourier domain OCT (FDOCT) setup (B) Spectral fringe pattern as detected by the CCD (left) and Fourier transformation of interferometric signal retrieving the reflectivity profile a(z) of the sample (right).

iii) Spectral domain OCT (SDOCT):

SDOCT is based on spectral interferometry, where recombined light from the reference and sample arms is spectrally dispersed and the spectral interference is recorded using a detector array. The detected interference signal at the spectrometer may be expressed as

$$I(k) = S(k)\left[a_R e^{i2kr} + \int_0^\infty a(z)\exp\{i2k[r+n(z)]\}dz \right]^2$$

where $S(k)$ is the source spectral intensity distribution, a_R is the backscattered amplitude of the reference beam, a(z) is the backscattered amplitude of the sample, n(z) is the refractive index. Assuming $a_R \sim 1$, this can be rewritten as

$$I(k) = S(k)\left(1 + \int_{-\infty}^{\infty} a(z)e^{i2knz}dz + \frac{1}{4}\int_{-\infty}^{\infty} AC[a(z)]e^{i2knz}dz \right)$$

It can be seen that I(k) has three terms: first term represents a constant offset; the third term represents the autocorrelation (AC) of the elementary waves within the sample; second term is the depth encoded amplitude, with the depth given by the frequency 2nz of the periodic function. Rewriting the spectral intensity distribution,

$$I(k) = S(k)\left(1 + \frac{1}{2}FT\{a(z)\} + \frac{1}{8}FT\{AC[a(z)]\} \right)$$

Where FT is the Fourier transform. An inverse FT of the spectral interferogram therefore retrieves the depth dependent scattering amplitude of the sample as given below:

$$FT^{-1}\{I(k)\} = FT^{-1}\{S(k)\} \otimes \left(\left[\delta(z) + \frac{1}{2}a(z) + \frac{1}{8}AC[a(z)] \right] \right)$$

where $\otimes$ represents the convolution function. The first term gives the FT of the source spectrum at z=0 and therefore can be separated from the signal by giving a small offset in the reference path. This source correlogram which appears as artifact in the SDOCT image can be removed by background subtraction with reference arm light only illuminating the detector. The AC terms are insignificant for highly scattering tissues. For high reflecting samples even from larger depths, the contribution of AC terms can be subtracted by taking a background signal illuminating sample only. It is to be noted that in FDOCT, the scattering amplitude along the depth of the sample (A-scan) is retrieved at once by the inverse FT.

Figure T.2.3A displays the schematic of SDOCT system, first referred to as "spectral radar". The SDOCT system utilizes a broadband light source in a Michelson interferometer where the interference spectrum is detected using a spectrometer. SDOCT can be understood by recalling that a Michelson interferometer acts like a periodic wavelength filter, where the periodicity is a function of the path difference between the sample and reference arms (figure T.2.3.B). The periodicity of this modulation will be inversely related to the echo time delay. The echo delays from the sample are measured by measuring the spectral distribution. Fourier transformation of the interference spectrum retrieves the axial (depth) information as shown in figure T.2.3.B (right). Note that Fourier transformation leads to negative frequency components also, but is not shown here. Lateral scanning only is done for generating the B-scan (image) of the sample. The DC and negative frequency components lead to artifacts in FDOCT images.

(iv) Swept-source OCT (SSOCT): Also referred to as optical frequency domain imaging (OFDI), figure T.2.4 (left) shows the basic configuration of SSOCT system using a tunable light source whose output is split into sample and reference paths. A square-law photo detector detects the interference between the reference and sample arm light while the wavelength of the monochromatic source is rapidly swept keeping the path lengths of the reference and sample arms constant. The Michelson interferometer interferes two frequency sweeps, which are time delayed with respect to each other and generates a beat frequency proportional to the path length mismatch ΔL (figure T.2.4, right).

The detector current can be expressed as

$$i_d = \frac{\eta q}{h\nu}\left(P_r + P_s\int r^2(z)dz + 2\sqrt{P_r P_s}\int r(z)\Gamma(z)\cos(2k(t)z + \phi(z))dz \right)$$

where η is the efficiency of the detector, q is the charge of the electron, $h\nu$ is the energy of the photon, P_r & P_s are the powers in the reference and sample beams, z is the axial

coordinate with z=0 implying zero optical path difference between the interfering beams, *r(z)* and *ϕ(z)* are the amplitude and phase of the reflectance profile of the sample, *Γ(z)* and k(t) are the coherence function and time varying wave number of the laser output respectively. The reflectivity profile along the axial direction (depth profile-both magnitude and position) is obtained by computing the Fourier transform of the sampled detector signals as in SDOCT. The advantage of SSOCT is that it uses a single detection channel. Like SDOCT, SSOCT also measures the echo signals from all depths at a time unlike in TDOCT where it is measured sequentially. This leads to a dramatic improvement in detection sensitivity and speed of acquisition. Figure T.2.5 displays the schematics of the fiber-optic implementation of all the three OCT modalities discussed above namely TDOCT, SDOCT and SSOCT. While TDOCT and SDOCT utilize broadband superluminescent diodes (SLD) as light sources, SSOCT requires a rapidly tunable swept source (SS). The tuning bandwidth determines the axial resolution in SSOCT systems.

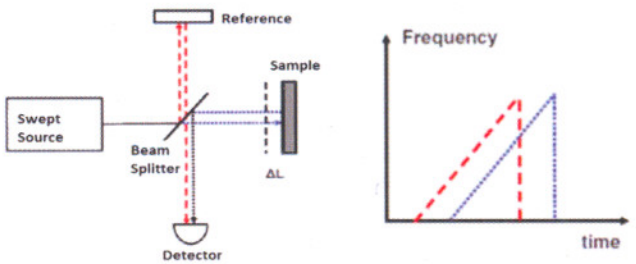

Fig T.2.4. Schematic of a frequency swept source OCT system using a Michelson Interferometer (left). Two frequency sweeps time delayed with each other leads to beat signal at detector due to a finite path length mismatch ΔL (right)

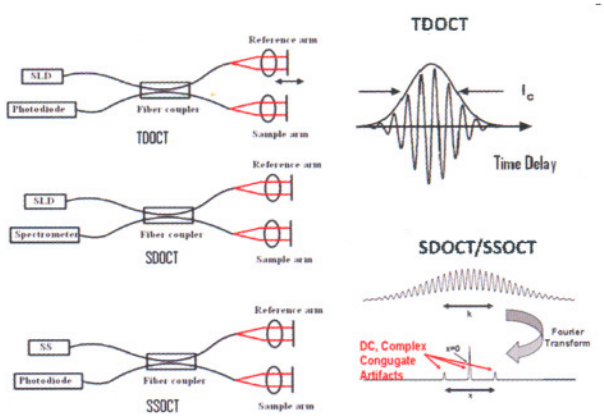

Fig T.2.5. Schematic of the three modalities of OCT: TDOCT, SDOCT, and SSOCT (left). SLD-Superluminescent diode; SS-swept source. The corresponding interferograms and demodulated profiles are shown on the right.

(v) Comparison of TDOCT & FDOCT methods: The axial resolution of FDOCT is inversely related to the bandwidth of the light source similar to TDOCT system. The range of imaging for TDOCT system is determined by the path-length scan of the reference mirror. For highly scattering samples such as biological tissues, light attenuation in the tissue restricts depth of imaging to 1-3 mm.

For SDOCT and SSOCT systems the range of imaging (δZ) is given by $\delta Z = \frac{1}{4n}\frac{\lambda^2}{\delta\lambda}$ where n is the refractive index of the medium, $\delta\lambda$ is the spectral resolution of the spectrometer for SDOCT system and wavelength sampling interval for SSOCT system respectively. Typically, the range of imaging for both SDOCT and SSOCT systems is designed to be greater than the penetration depth in the tissue at the corresponding wavelength. The SNR of the FDOCT system is given by

$$SNR_{FDOCT} = \frac{\langle i_d \rangle^2}{\sigma^2} = \frac{\rho S_{FDOCT}[k_m] R_S}{4eB_{FDOCT}} M$$

where M is the no. of detector channels, $S_{FDOCT}[k_m]$ is the instantaneous power incident on the sample corresponding to spectral channel m. It can be easily seen that the SNR_{FDOCT} is a factor M/2 higher compared to SNR_{TDOCT} assuming source has equal power in all spectral channels. Assuming $M \sim 10^3$, it can be shown that the FDOCT systems are in principle capable of up to 20 dB greater sensitivity than the TDOCT systems. Further, rapid advances in generation of tunable sources and high-speed line scan arrays resulted in the faster rate of acquisition of axial scans for FDOCT setups by a factor ~10 compared to the conventional TDOCT systems.

Despite the SNR and speed advantages, the FDOCT schemes require computational tasks such as spectral sampling in k-space, discrete Fourier transformation etc. Further, image artifacts at DC and negative frequencies (known as complex conjugate artifacts) limit the actual imaging depth. Removal of complex conjugate artifacts not only requires sophisticated signal processing/hard-ware implementations, they also lead to decreased sensitivity and speed. While the DC artifact in the images can be removed by subtracting the pre-acquired DC spectrum by keeping reference light only, the negative frequencies can be suppressed to double the imaging depth, by reference phase-shifting using a piezo stage in reference arm. The SNR in SDOCT systems degrade with depth due to fringe washout caused by pixel cross talk and finite spectral resolution of CCD. Similarly non-linearity in the frequency sweep of the swept laser results in chirping of the signal and causes a degradation of axial resolution requiring the use of sophisticated signal processing methods in SSOCT.

(vi) Full field OCT (FFOCT): In FFOCT, entire field of the sample is illuminated with a low spatial coherence light

source and full field interferometric images acquired in parallel using a CCD or CMOS detector are used to generate tomographic enface images (orthogonal to optic axis). FFOCT, sometimes also referred to as full-field optical coherence microscopy (OCM), is essentially an interference microscope illuminated by a white-light source such as a tungsten-halogen lamp. The transverse resolution of FFOCT is similar to that of a conventional microscope and with the use of high NA microscopic objectives one can easily get transverse resolution ~1 μm. This is an advantage compared to the TD and FD OCT techniques where the use of high NA objective leads to a reduced depth of imaging as cross-sectional images are acquired. The axial resolution of FFOCT is determined by the coherence length of the light source and since the spectrum of thermal light sources used in FFOCT is smooth and broad, sub-micron axial resolution is indeed demonstrated with FFOCT after due compensation of dispersion in the system. Very recently FDA approved commercial instrument based on FFOCT is launched for clinical diagnosis with histological resolution.

3. Functional Extensions of OCT:

(i) Doppler OCT (DOCT): This is also known as Optical Doppler Tomography and is a functional extension of OCT that enables quantitative noninvasive measurement of depth resolved-blood flow in tissues in addition to the microstructure of the tissue. The backscattered light from a moving scatterer like that from a blood cell will be frequency shifted with respect to the incident light and beats with the reference light resulting in Doppler frequency given by $w_D = K.v_s$ where K is the wave vector and v_s is the velocity of the scatterer (Figure T.2.6).

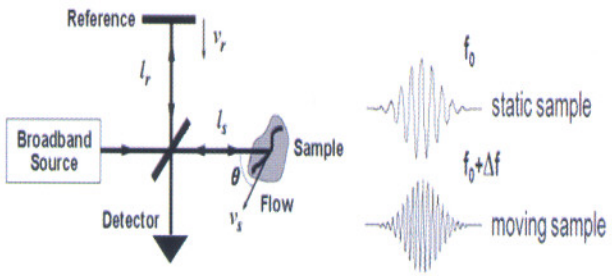

Fig T.2.6. Schematic of Doppler OCT (left) and interferograms with static and moving sample (right)

The cross-correlation function R_{rs} at the detector is given by

$$R_{rs}(t) = A(t)\cos[2\pi(f_r - f_s)t + \varphi(t)]$$,where

A(t) is the amplitude of the interferogram, f_r and f_s are the frequencies of light returning from the reference and sample beams given by $f_r = 2v_r/\lambda$, $f_s = 2v_s n_t \cos(\vartheta)/\lambda$, $\varphi(t)$ is the position of the scatterer and ϑ is the scatterer angle with respect to the incident light. By use of short-time fast Fourier transform (STFT) of the coherently demodulated interferomteric signal, Izatt et al [7] retrieved depth localized Doppler signal in addition to the conventional intensity information. Depth resolution of the velocity depends on the STFT window length. In order to provide increased sensitivity to small flows, DOCT can also be implemented by measuring phase changes in sequential axial scans. Typical velocity resolutions are in the range of few μm/s. At present, the maximum probing depth of the OCT system limits imaging to blood vessels close to the surface of highly scattering tissues. In addition to measuring retinal blood flow in-vivo, DOCT has also been used in dermatology to analyze the structure of blood vessels in port wine stain photocoagulation, for in vivo monitoring of photodynamic therapy and in developmental biology for monitoring the cardiac flow dynamics.

(ii) Polarization sensitive OCT (PSOCT):

Several tissue constituents such as collagen, muscle, nerve fibers, tendon, cartilage, bones etc are birefringent. The birefringence in the tissue caused either by the anisotropy of constituent molecules (intrinsic) or by the ordered layering (form) of anisotropic structures provides an alternative contrast mechanism in OCT which can be linked to the function and status of the tissue compared to the intensity based OCT. The birefringence changes in the tissue could be measured in a polarization sensitive OCT (PSOCT) scheme, by examining the polarization properties of the scattered light. PSOCT is implemented in two approaches- either by a dual detector setup for measuring the orthogonal polarization components in the scattered light or by use of a single detector with dual reference beams.

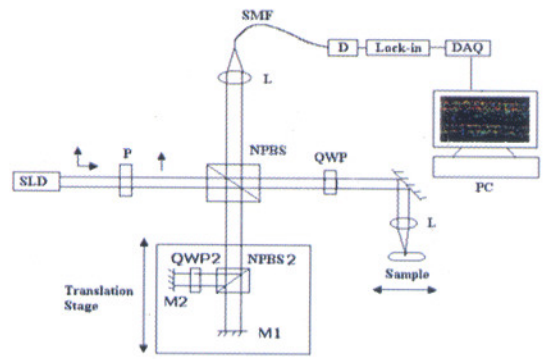

Fig T.2.7. Schematic of a free space PSOCT system.SLD-Superluminescent diode; NPBS-Nonpolarizing beam splitter; QWP-quarter wave plate; SMF-single mode fiber.

Figure T.2.7 shows a typical bulk-optic based PSOCT scheme implementing a single detector based approach. The interferometer is illuminated with a linear vertical state (V) polarized light. The reference path is split in to two beams by a non-polarizing beam splitter (NPBS). One of the reference

arm beams was passed through a quarter wave plate (QWP) with 45° orientation to get horizontally (H) polarized light on round trip. The H and V polarized reference beams were reflected with two mirrors M1 and M2 with a delay. The sample path contains a QWP oriented at 45° wrt to H thus illuminating the tissue with a circularly polarized beam. The sample returns an arbitrary elliptical polarization which after beating with the dual reference beams generates at the detector two interferograms pertaining to the H and V components. The retardation image is computed using the intensity values of the H (I_H) and V (I_V) components and is given by.

$$\delta(z) = \sqrt{\arctan(I_V(z)/I_H(z))}$$

Fiber-optic high speed implementation of PSOCT has also been established both in TDOCT and FDOCT systems [4]. PSOCT has been used to quantify the health of retina by measuring the birefringence changes in the nerve fiber layer. In dental tissues, the intensity of cross polarized light was shown to be directly correlated with the degree of demineralization of teeth and severity of caries. PSOCT is also being used in monitoring the wound healing as reorganization of collagen matrix leads to birefringence changes.

(iii) Molecular contrast OCT (MCOCT):

Molecular contrast agents commonly used in fluorescence, confocal, multiphoton microscopy techniques cannot be directly incorporated in OCT due to the incoherent scattering process. The MCOCT techniques that have been implemented till date can be categorized as absorption modulation, scattering modulation and coherent emission methods [4]. The absorption modulation methods include pump-probe OCT, pump suppression OCT and spectroscopic OCT. The coherent emission methods include second harmonic generation (SHG OCT), coherent anti-stokes Raman scattering (CARS OCT). The scattering modulation methods use either microscopic particles tailored to strongly scatter light or nano contrast agents such as magnetic nano particles or Plasmon resonant nano probes. Despite successful demonstration of these techniques in tissue phantoms & tissues, technological challenges remain to be overcome before any of these methods could be used for targeted *in vivo* clinical imaging.

4. Representative applications of OCT for Tissue Diagnosis:

(a) ***In vivo*** **small animal imaging:** Figure T.2.8 shows a schematic of a slow speed OCT setup developed at RRCAT. The output of superluminescent diode (SLD) with a center wavelength of ~840 nm was coupled into a fiber optic based Michelson interferometer by use of a 2x2 beam splitter designed for the wavelength used. The light beam in the sample arm was collimated and focused on to the sample with a 10X microscopic objective. The reference mirror was mounted on a linear translation stage and scanned back and forth with a uniform velocity to result in a Doppler shift of 45 kHz The light reflected from both the sample and reference arms was detected by a photodiode (PD), and the resulting interferogram demodulated using a Lock-in amplifier. The interferogram envelope was acquired in a PC using a data acquisition card (DAQ). Lateral scanning was done using a stepper motor. The free space axial and lateral resolutions of the setup were estimated to be ~11 µm and 17 µm respectively. The signal to noise ratio (SNR) of the setup was measured to be ~100dB. Typical image (500x100 pixels) acquisition time was about 1 minute. The OCT images have been false-color coded such that white represents highest backscattering intensity.

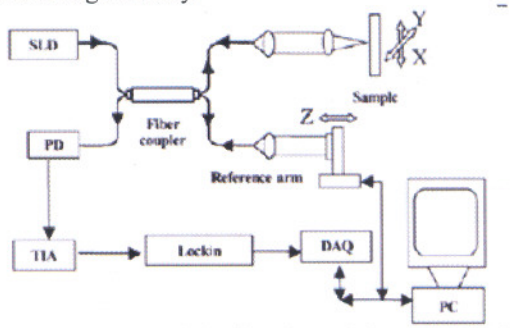

Fig T.2.8. Schematic of the fiber-based slow-speed OCT setup developed at RRCAT. SLD-Superluminescent diode; PD-Photodiode; TIA-Transimpedence amplifier; DAQ-data acquisition board.

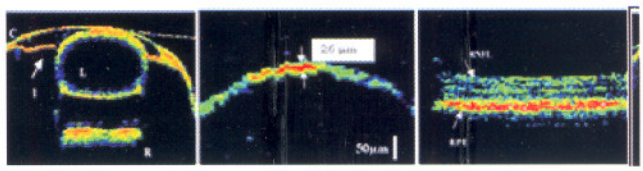

Fig T.2.9. OCT images of ocular structures of Zebrafish (whole eye(left), cornea (middle) and Retina (right) ;C-cornea, L-lens, R- retina, RPE-retinal pigment epithelium, RNFL-retinal nerve fiber layer;

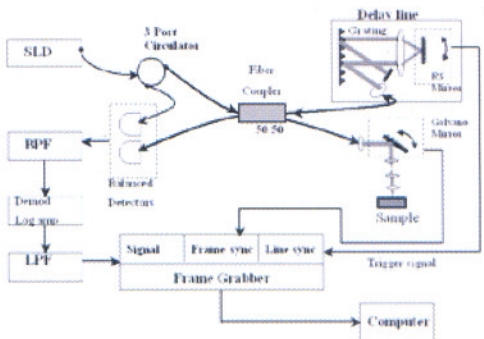

Fig T.2.10. Schematic of the time-domain based fiber-optic real-time OCT setup developed at RRCAT. SLD-Superluminescent diode; BPF-Bandpass filter; LPF-Low pass filter;

Images of whole eye, cornea and retina (Figure T.2.9) acquired with the set-up have been used to estimate several ocular parameters, viz. corneal thickness, mean retinal thickness and effective refractive index of the crystalline lens [8]. Further, use of OCT for noninvasive measurement of gradient refractive index profile was also investigated, as axial scans in OCT give the optical path rather than the geometric path. This method retrieves the parameters of the polynomial form gradient refractive index profile by iterative fitting of optical path calculated by ray tracing method with that experimentally measured using OCT. The approach has been employed for determining the index profile of fish eye lens under *in-vivo* conditions [9].

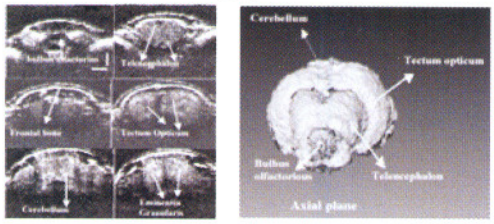

Fig T.2.11. 2-D cross sectional OCT images showing internal structures of Zebrafish brain (left). Scale bar is 0.5 mm. 3D reconstructed view of the Zebrafish brain.

The real-time OCT system developed at RRCAT (figure T.2.10), utilized a high power broadband superluminescent diode (SLD) optical source coupled to single mode fiber (λ_0=1310 nm, $\Delta\lambda$=43 nm, power~ 18mW). A Fourier domain based rapid scanning optical delay line (scanning frequency of 2 kHz) was used in the reference arm to achieve path length scan of about 3 mm. Lateral scanning was done @ 8 Hz using a single-axis galvanometer-driven mirror. The free space axial and lateral resolutions of the set up were both estimated to be 20 µm. This set up was used to acquire two-dimensional cross sectional images of the adult brain of anaesthetized Zebrafish. About 90 cross-sectional images (XZ plane) of the brain were taken by moving the sample in the Y direction in a step of 0.05 mm. Figure T.2.11(left) show the 2-D cross-sectional images of Zebrafish brain. Internal structures such as bulbus olfactorius, telencephalon, tectum opticum, cerebellum, frontal bone and eminentia granularis were clearly distinguishable in these images. The raw images were thresholded for minimizing the speckle noise. Using these images, a three-dimensional iso-surface model of the Zebrafish brain was constructed in the axial plane (Figure T.2.11 right) [10].

OCT is also being used for studying developmental biology. A real time SDOCT system was used to monitor ethanol-induced developmental defects in zebrafish embryos/larvae [11]. Figure 12 shows the schematic of the SDOCT setup. Light from a superluminescent diode (SLD) was coupled to a Michelson interferometer through a fiber optic coupler (FOC). The light reflected from the sample and reference arms was spectrally dispersed using a transmission grating and imaged onto a line scan camera for real time acquisiton and display of images. The zebrafish embryos were exposed to ethanol at varying concentrations in the range 150-350mM for 48 hours post fertilization and OCT imaging was performed at regular intervals both on unexposed (controls) and ethanol treated samples. The study showed prominent changes in the internal structure of the eye including shrinkage of the eye and less featured retinal bands in the ethanol exposed samples (figure T.2.13A). Also the diminished light scattering observed from retinal layers indicated morphological alterations in retina. Further, the ethanol exposed larvae showed malformations in the spinal chord as evidenced by the distortions in the notochord and bending of tails (figure T.2.13B). As there is a growing interest in attenuating the deleterious effect of toxins through use of anti-oxidants, OCT imaging may prove to be a valuable tool in the study of developmental toxicology and drug screening.

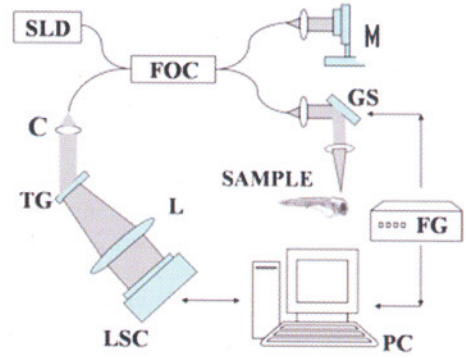

Fig T.2.12. Experimental setup for real time SDOCT imaging. C- collimator; FG- function generator; FOC-fiber optic coupler; GS- galvascanner; L- lens; LSC-line scan camera; M -mirror; SLD-superluminescent diode; TG- transmission grating;

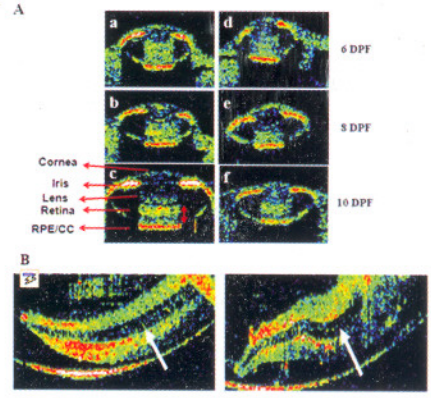

Fig T.2.13. (A) OCT images of eye development of zebrafish control (left panel) and ethanol exposed (right panel) larvae for different days post fertilization (dpf). (B) Tail of the control (left) and 350mM ethanol exposed (right) zebrafish larvae at 10dpf.

(b) OCT imaging of tumor tissues:

(i) Imaging of tumor spheroids: Multi-cellular tumour spheroids are three-dimensional cell cultures, which resemble avascular solid tumors. Tumor spheroids exhibit structural, metabolic, and functional and growth pattern similarities to solid tumors and are therefore a good model systems for studying therapeutic effects of radiation. These are also being increasingly used for studying response of solid tumors to photodynamic therapy and for studies directed towards understanding tumor growth, and cell biology. For studying the response of tumor spheroids to drugs, noninvasive techniques that could periodically monitor the size and the shape of spheroids are required. Conventional light microscopy cannot be used to measure the depth of the sample and hence volume estimations lead to large errors. Sharma et al [12] demonstrated the use of OCT imaging for studying the dynamics of spheroid formation and accurate estimation of tumor volume compared to light microscopy. Volume of spheroids estimated by this method correlated well with the increase in cell number as a function of the growth.

(ii) Imaging of resected human breast tissues: The resolution of standard OCT systems (~10 μm) is not sufficient to resolve the cytological differences in the tissues. However the onset of disease induces changes in scattering properties of the tissues that can be detected by image analysis using various computational algorithms. (fig.T.2.14) shows representative OCT images of resected human breast tissues of normal (adipose), benign (fibroadenoma) and malignant (invasive ductal carcinoma) pathologies. Significant differences in the texture of scattering pattern for different types of breast tissue samples are apparent. The cell structure of normal fatty (adipose) tissue is seen to be well resolvable. In contrast to the low-scattering regions of adipocytes of normal tissue, the benign and malignant samples, due to the solid tumor, showed relatively dense and smooth scattering with the scattering intensity slightly higher for malignant tissues as compared to the benign ones. Bhattacharjee et al [13] used computational algorithms for binary tissue classification (normal versus abnormal; malignant versus benign) with significantly high sensitivity and specificity.

Fig T.2.14 Representative OCT images of resected human breast tissues of different pathologies.

(c) In vivo oral tissue imaging:

In vivo imaging of oral tissues is another promising area where OCT images could help diagnose the oral lesions at an early stage. Figure T.2.15 shows OCT image (bottom) of buccal mucosa of healthy human subject *in vivo* taken with a handheld probe (top) of a real time TDOCT system described above [14]. OCT image clearly delineates different layers of the healthy mucosa namely the stratified squamous epithelium, lamina propria and submucosa that could be correlated to histology. Invasion of the tissue by disease alters the microanatomy that could be tracked using OCT for development, transformation and progression of disease. Several clinical trials have demonstrated the potential of OCT in early detection and diagnosis of oral lesions. OCT could be a powerful tool in rapid screening of suspected population for oral cancer and therapeutic efficacy of the treatment modalities.

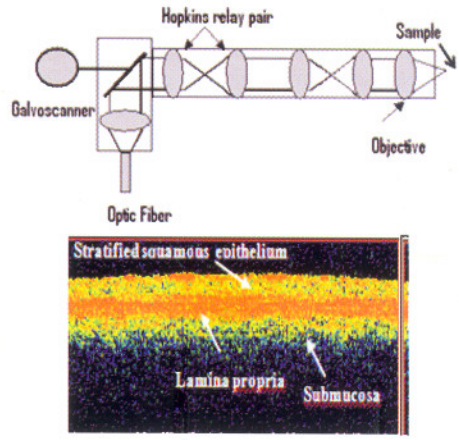

Fig T.2.15 Schematic of an oral probe (15mm dia) integrated with a real time TDOCT system (top) and OCT image of buccal mucosa of a healthy human subject in vivo (bottom).

(d) OCT for Birefringence imaging:

As mentioned earlier, monitoring the birefringence changes give valuable information about the collagen and hence the function of the tissue. PSOCT has been recently used for imaging of malignant (invasive ductal carcinoma), benign (fibroadenoma) and normal (adipocytes) breast tissue samples [15]. The results of this study showed that while conventional OCT is able to discriminate breast tissues as normal (adipocytes) and abnormal (malignant and benign) tissues, PSOCT helps in discriminating between malignant and benign tissue sites also due to the large birefringence of the benign samples compared to the malignant ones. This observation could lead to an improved tissue classification between benign and malignant tissues.

In a recent report, OCT and PSOCT imaging was carried out for monitoring the healing of superficial wounds infected with bacteria *Staphylococcus aureus* in mice under in vitro and in vivo conditions for studying the changes in collagen birefringence in the infected wounds [16]. From the

OCT and PSOCT images, different phases of wound healing such as inflammation, reepithelialization and collagen remodeling could be identified. The edematic regions appeared prominent in infected wounds. Compared with uninfected wounds, reepithelization and collagen remodeling phases of wound healing were delayed significantly in the infected wounds.

5. Current Limitations of OCT and Future Scope:

OCT is a powerful imaging technology that has made rapid progress in recent years. Currently OCT is routinely used in ophthalmology for diagnosis of various retinal diseases. Some of the limitations of OCT at present are low penetration depth, poor resolution, and lack of compatible fiber probes to reach internal organs. Despite the low penetration depth of ~1-3 mm in highly scattering tissue, OCT techniques offer superior resolution compared to ultrasound or MRI for clinical diagnosis. However compared to histopathology, the resolution of standard OCT systems is nearly an order of magnitude poorer. Development of cheap table top ultra-broadband light sources may lead to ultra-high resolution images matching histology without necessitating excisional biopsy for disease diagnosis. Early detection of morphological and functional changes in the tissue at a precancerous stage remains a challenge to overcome in the coming years. With rapid developments in the high speed acquisition and processing of data, obtaining volumetric data set in near real time is a distinct reality. This will open up large scale clinical studies to be undertaken for 3-D sub-surface microanatomy for tissue diagnosis. Availability of huge sample data set provides an additional challenge in terms of image interpretation and tissue diagnosis. Several groups have been investigating the use of automated tissue classification algorithms and with a suitable diagnostic algorithm in place, OCT imaging is expected to aid the clinician for in situ optical biopsy and also during intra-operative procedures for identification of surgical margins. Ongoing innovations include multimodal optical systems integrating laser induced fluorescence and laser Raman spectroscopy setups with OCT systems for simultaneous interrogation of the tissue. With such multimodal OCT systems, biochemical and molecular specific information of the tissue could also be obtained along with the structural information enhancing the diagnostic potential of the optical technologies. Finally, it is not an unrealistic proposition to visualize a multi-modal and multi-functional OCT imaging system that is integrated with the existing clinical modalities for providing high resolution images of morphological, biochemical, molecular and functional information for early disease diagnosis and quality health care. OCT is therefore poised to be a valuable tool for disease diagnosis in the years to come.

Acknowledgements:

The author would like to thank Shri Y. Verma, Dr. M. Sharma, Shri H. S. Patel, Shri K. Sahu, Shri M. K. Swami, Dr. S. K. Majumder and Ms. P. Sharma for their valuable contributions at different stages of the experiments described in this article. The author also would like to thank Dr. P. K. Gupta for his keen interest and constant support.

References :

1. D. Huang, E. A. Swanson, C.P. Lin, J. S. Schuman, W. G. Stinson, W. Chang, M. R. Hee, T. Flotte, K. Gregory, C. A. Puliafito, and J. G. Fujimoto, Science 254, 1178-1181 (1991).
2. B. E. Bouma, and G. J. Tearney (Eds.), Handbook of Optical Coherence Tomography, (New york:Dekker, 2002)
3. A. Gh Podoleanu, The British journal of Radiology 78, 976 (2005)
4. W. Drexler and J. G. Fujimoto (Eds.), Optical Coherence Tomography: Technology and Applications,(Springer-Verlag Berlin Heidelberg 2008)
5. A.F. Fercher, Z. Med. Phys. 20, 251 (2010)
6. J. A. Izatt, M. D. Kulkarni, K. H. Wang, K. Kobayashi and M. V. Sivak IEEE J. Select. Top. Quant. Electron. 2, 1017-28 (1996)
7. J. A. Izatt, M. D. Kulkarni, S. Yazdanfar, J. K. Barton and A. J. Welch Opt. Lett. 22, 1439-41 (1997)
8. K. D. Rao, Y. Verma, H.S. Patel and P.K. Gupta, Current science 90, 1506 (2006)
9. Y. Verma, K. D. Rao, M. K. Suresh, H. S. Patel, and P. K. Gupta, Applied Physics B 87, 607 (2007)
10. K. Divakar Rao, A. Alex, Y. Verma, S. Thampi, and P. K. Gupta, J. Biophotonics 2,288 (2009)
11. K. Divakar Rao, P. Upadhyaya, M. Sharma, and P. K. Gupta, Birth Defects Research B: Developmental and Reproductive Toxicology, In Press (2011).
12. M. Sharma, Y. Verma, K. D. Rao, R Nair, and P. K. Gupta, Biotechnolgy Letters 29, 273 (2007)
13. M. Bhattacharjee, P. C. Ashok, K. Divakar Rao, S. K. Majumder, Y. Verma, and P. K. Gupta, J. Innovative Opt. Health Sciences 4, 59-66 (2011)
14. A. Alex, M.Sc Dissertation, CUSAT Cochin (2007)
15. Y. Verma, M. Gautam, K. Divakar Rao, M. K. Swami and P. K. Gupta, Laser Physics 21, 2143-48 (2011)
16. K. Sahu, Y. Verma, M. Sharma, K. D. Rao and P. K. Gupta, Skin Research & Technology 16,428-37 (2010)